

pubs.acs.org/JPCC Article

# Synergy of Carbon Nanotube-Supported Bimetallic Nanoalloy Catalysts in Rechargeable Lithium—Oxygen Batteries

Published as part of The Journal of Physical Chemistry virtual special issue "Zhao-Wu Tian Festschrift". Ren Na, Merry N. Madiou, Dominic Caracciolo, Zhi-Peng Wu, Connor Kanyuk, Guojun Shang, and Chuan-Jian Zhong\*



Cite This: J. Phys. Chem. C 2023, 127, 13547-13555



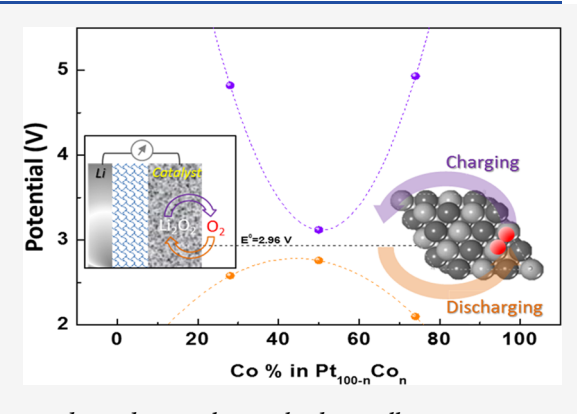
ACCESS I

Metrics & More

Article Recommendations

Supporting Information

ABSTRACT: The ability to tune the electrocatalytic activities of oxygen reduction and evolution reactions at the air cathode is essential to reduce the overall overpotentials of rechargeable Li-air batteries. This report demonstrates a pathway to this ability by engineering the bimetallic composition of nanoalloy catalysts. This involves alloying Pt with oxyphilic Co in different bimetallic compositions by hydrothermal synthesis of the bimetallic alloy nanoparticles on carbon nanotubes, i.e., Pt<sub>100-n</sub>Co<sub>n</sub>/CNT. The catalysts are characterized by different techniques, showing facecentered cubic alloy characteristics with crystalline and less-crystalline/ amorphous domains. The degree of oxidation of the Co components in the nanoalloys depends on the bimetallic composition, which is linked to the oxygen capacity of the nanoalloys. By discharging/charging performance testing in a rechargeable Li-O<sub>2</sub> battery cell, the overpotentials for oxygen



evolution reaction (OER) and oxygen reduction reaction (ORR) are shown to depend strongly on the bimetallic composition. Pt<sub>50</sub>Co<sub>50</sub>/CNT shows the lowest ORR and OER overpotentials, 160–170 mV, with respect to the thermodynamic potentials of Li/ Li<sub>2</sub>O<sub>2</sub>. This catalytic synergy is discussed in terms of the oxyphilicity of the catalysts, along with the calculated oxygen adsorption energies.

## 1. INTRODUCTION

Rechargeable Li-air batteries exhibit a high energy density, which can provide power for electric vehicles. The charge and discharge processes,<sup>2,3</sup> including the oxygen evolution reaction (OER) and oxygen reduction reaction (ORR) in the air cathode, have been studied in different types of electrolytes, particularly aprotic electrolytes, in the Li-air battery. The ORR involves 2e reduction of O<sub>2</sub> at the cathode, which reacts with Li ions from the lithium anode forming lithium peroxide  $(Li_2O_2)$ , whereas the OER involves 2e oxidation of  $Li_2O_2$ , releasing  $O_2$  and  $Li^+$ . While the thermodynamic potential for the charge/discharge cycle is 2.959 V,4 the sluggishness of the OER process results in high overpotential, leading to a significant loss in performance in terms of rate capacity and long-term stability.<sup>5</sup> The ultimate commercialization of rechargeable Li-air batteries must address various challenges, including poor electrochemical performance, low coulombic efficiency, and short cycle life, 6,7 especially at the air cathode.8 To reduce the overpotential and increase the cycle life, noble metals such as Pt, Ir, and Ru are often used as catalysts for the air cathode. 9-12 Alloying noble metals with other transition metals has been explored in order to improve the performance of noble catalysts, including, for example, PtCo alloy catalyst

showing a maximum capacity of 3040 mAh  $\rm g^{-113}$  and PtAu catalyst showing 1200 mAh  $\rm g^{-1}$ . The AuPt alloy catalysts are shown to exhibit a bifunctional catalytic activity responsible for enhancing both ORR and OER kinetics. 15,16 PdCu alloy catalysts also display a reduced overpotential and a significant increase in the discharge capacity due to the synergy effect of Pd and Cu. 17

The formation of Li<sub>2</sub>O<sub>2</sub> is a key step in the ORR. Its deposition on the catalyst surface could block the active sites of the catalyst. 18,19 Cobalt exhibits a higher oxophilicity than platinum, which could play a role in manipulating the deposition of Li<sub>2</sub>O<sub>2</sub> on the surface, preventing the active site from being blocked or deactivated. 20 The presence of Co and Pt atoms in a random surface alloy state could produce a bifunctional catalytic synergy in which the Pt site activates molecular oxygen whereas the Co site enables the removal or

Received: May 2, 2023 Revised: June 19, 2023 Published: July 7, 2023





relocation of the intermediate -OLi species on the surface in the ORR process. In the OER process, the Co site may facilitate the transfer of the oxygenated species to the Pt site for activation and subsequent oxidation to molecular oxygen. 13,21,22 Despite the significant progress, a key problem in rechargeable Li-air batteries is the lack of understanding of how a solid catalyst catalyzes the formation and decomposition of solid Li<sub>2</sub>O<sub>2</sub>, especially the confronting passivation and loss of catalyst-Li<sub>2</sub>O<sub>2</sub> contact, in the discharging/charging processes. Recently, the structural change at the RuO2 (catalyst)/Li<sub>2</sub>O<sub>2</sub> interface during discharging and charging is examined by an operando scanning transmission electron microscopy (STEM) study in a Li-O<sub>2</sub> microbattery.<sup>23</sup> RuO<sub>2</sub> is believed to serve as the site for Li<sub>2</sub>O<sub>2</sub> deposition during the discharging process. Catalytic activation of RuO2 is required for the decomposition of the precipitated Li<sub>2</sub>O<sub>2</sub> and their dissolution via a chemical comproportionation reaction. An increasing amount of Li<sub>2</sub>O<sub>2</sub> nanoparticles (NPs) on the RuO<sub>2</sub> surface and the gold electrode is revealed during the discharging progress, which continuously grow after passing the nucleation stage. Continuous discharging leads to a complete encapsulation of the RuO2 NPs by Li2O2. In the subsequent charging process, there is no indication of dissolution of Li<sub>2</sub>O<sub>2</sub> around the encapsulated RuO<sub>2</sub> particles and surrounding Li<sub>2</sub>O<sub>2</sub>/electrolyte interfaces, consistent with the passivation of the RuO<sub>2</sub> NPs by the insulative Li<sub>2</sub>O<sub>2</sub> particles. Upon continuous charging, there is a movement of the reaction frontier along the gold electrode showing a gradual spreading to the Li<sub>2</sub>O<sub>2</sub> capped RuO<sub>2</sub> NPs and a gradual exposure of RuO2 NPs to the electrolyte. The contact of the RuO<sub>2</sub> particles on the gold electrode with the electrolyte allowed for a quick dissolution of the Li2O2 phase at the Li<sub>2</sub>O<sub>2</sub>/RuO<sub>2</sub> interface, thus recovering the RuO<sub>2</sub>'s catalytic activity at the triple RuO<sub>2</sub>/Li<sub>2</sub>O<sub>2</sub>/electrolyte interfaces driven by the dilution of LiO2 and enrichment of active oxygen in the surrounding electrolyte. The formation of the solvable LiO2 product is an intriguing pathway to avoid the immediate passivation of the catalyst by Li<sub>2</sub>O<sub>2</sub>. Based on this finding, the high charging overpotential is hypothesized to depend on the metal-oxygen structure and composition at the surface of the catalyst, which determines the decomposition rate. In this report, we demonstrate that the charging overpotential can be significantly reduced by optimizing the composition of PtCo NPs supported on carbon nanotubes (CNTs) in terms of oxygen adsorption and release capacity at the catalyst/Li<sub>2</sub>O<sub>2</sub>/ electrolyte interfaces, a design strategy to overcome the confronting passivation and reactivation of the catalyst in the discharging/charging processes.

## 2. EXPERIMENTAL SECTION

**2.1.** Chemicals. Platinum acetylacetonate (Pt(acac)<sub>2</sub>, 97%), cobalt acetylacetonate (Co(acac)<sub>2</sub>, 98%), *N*,*N*-dimethylformamide (DMF), and Nafion (5 wt %) were purchased from Sigma-Aldrich. Carbon nanotube (CNT) with a diameter of 10–20 nm and length of 1–2  $\mu$ m was obtained from Shenzhen Nanotech PortCo., Ltd. A 1M lithium hexafluor-ophosphate electrolyte in a 1:1 solution of ethylene carbonate and dimethyl carbonate (LiPF<sub>6</sub> in EC/DMC) and pure lithium foil with a diameter of 15.6 mm were obtained from MTI. Ethanol, 2-propanol, perchloric acid, and potassium chloride were purchased from Fisher Scientific. The deionized water (18.2 MΩ) obtained by the purification system was used. N<sub>2</sub>, O<sub>2</sub>, and Ar were obtained from Airgas. All of the chemicals

were used as received without further purification. The CNTs were obtained from Shenzhen Nanotech, which are fibrous, porous, and conductive.

- **2.2.** Synthesis of PtCo/CNT. Pt<sub>100-n</sub>Co<sub>n</sub>/CNT catalysts were synthesized by a hydrothermal method in which the two metal precursor feeding ratio was controlled (e.g., 25, 50, and 75% Co). Briefly, 100 mg of CNTs was dispersed into 50 mL of DMF by sonicating for 0.5 h. Then, platinum acetylacetonate and cobalt acetylacetonate in a controlled molar ratio were added to the above suspension, followed by sonicating for another 0.5 h and stirring for 15 min. Afterward, the mixture was transferred to a Teflon-lined autoclave and was heated at 180 °C for 24 h. The product was washed with ethanol several times followed by centrifuging to precipitate and dried in a vacuum oven overnight.
- **2.3. Structural Characterizations.** The chemical composition of PtCo/CNT was analyzed by inductively coupled plasma optical emission spectroscopy (ICP-OES) using a PerkinElmer 2000 DV ICP-OES instrument. The microstructure of the sample was characterized by transmission electron microscopy (TEM) and high-resolution transmission electron microscopy (HRTEM, JEM-2100F). The X-ray diffraction (XRD) was used to analyze the crystal structure of the sample with Cu K $\alpha$  radiation ( $\lambda$  = 1.5406 Å) and the data were collected from 20 to 90° 2 $\theta$  with a step size of 0.033° at room temperature. Thermogravimetric analysis (TGA) was conducted from room temperature to 800 °C to analyze the metal loading of the as-obtained catalyst. The surface composition and chemical state of the PtCo/CNT were characterized by XPS (PHI 5000 Versa Probe).
- **2.4. Electrochemical Measurement.** A glassy carbon (GC) disk was polished using 1 and 0.05  $\mu$ m Al $_2$ O $_3$  powder before use. The catalyst ink was prepared by suspending 10 mg of PtCo/CNT into 5 mL of deionized water containing 2-propanol and Nafion, followed by sonicating for 30 min in an ice bath to obtain well-dispersed ink. Then, 15  $\mu$ L of ink was dropped on the GC and dried at room temperature. The cyclic voltammetry (CV) and rotating disk electrode (RDE) measurements were conducted using an electrochemical workstation (CHI620a, CH Instruments). A Pt wire was used as the counter electrode and a reversible hydrogen electrode (RHE) filled with 0.1 M HClO $_4$  was used as the reference electrode.

For a Li– $O_2$  battery, the battery was assembled in a glove box with  $H_2O$  and  $O_2$  content below 0.01 ppm. Pure lithium foil (MTI, diameter of 15.6 mm) was used as the counter and reference electrodes. The working electrode was prepared by coating the ink on the carbon paper with a catalyst loading of 1 mg cm $^{-2}$ . The electrolyte used here is 1 M lithium hexafluorophosphate electrolyte in a 1:1 solution of ethylene carbonate and dimethyl carbonate (LiPF $_6$  in EC/DMC). Celgard C480 (Celgard) was used as the separator. A stainless-steel mesh was employed as the current collector. The assembled battery was purged with TEGDME-saturated oxygen for 10 min before testing. Discharging/charging measurements were conducted on an electrochemical work-station (Biologic SP-150).

#### 3. RESULTS AND DISCUSSION

**3.1. Composition, Morphology, and Structure Characterizations.** The bimetallic composition of  $Pt_{100-n}Co_n/CNT$  catalysts was controlled by the feeding ratio of the metal precursors and the reaction temperature (Figure 1). The actual

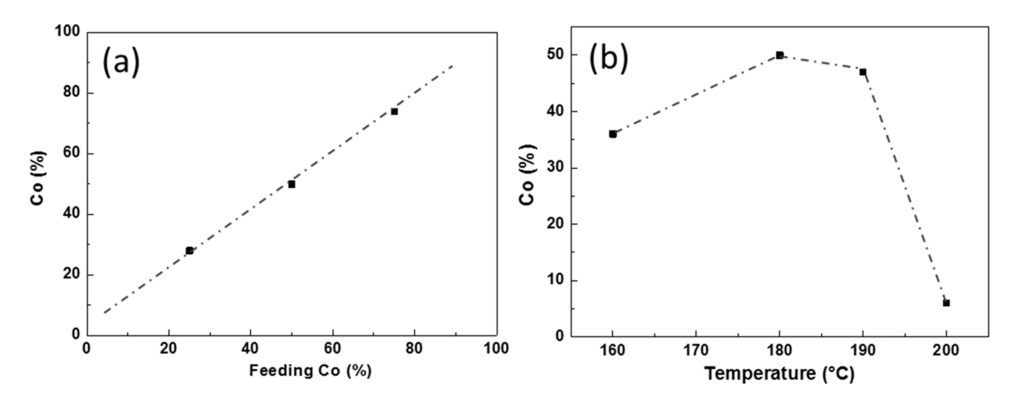


Figure 1. (a) Plot of NP's Co%—feeding Co% and (b) plot of NP's Co%—reaction temperature for the  $Pt_{100-n}Co_n/CNT$  catalysts synthesized at 180 °C with different metal feeding ratios (a), and at different temperatures with the same 50:50 metal feeding ratio (b).

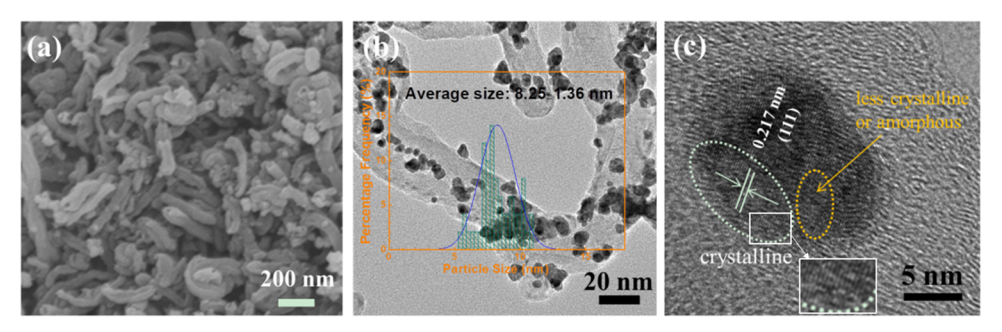


Figure 2. Images of (a) SEM, (b) TEM, and (c) HRTEM of  $Pt_{50}Co_{50}/CNT$ . In panel (b), the size distribution of the NPs on CNTs (8.3  $\pm$ 1.4 nm) is shown. Panel (c) shows the lattice fringe d(111) = 0.217 nm, which approximately corresponds to an fcc-lattice constant (a) of 0.372 nm.

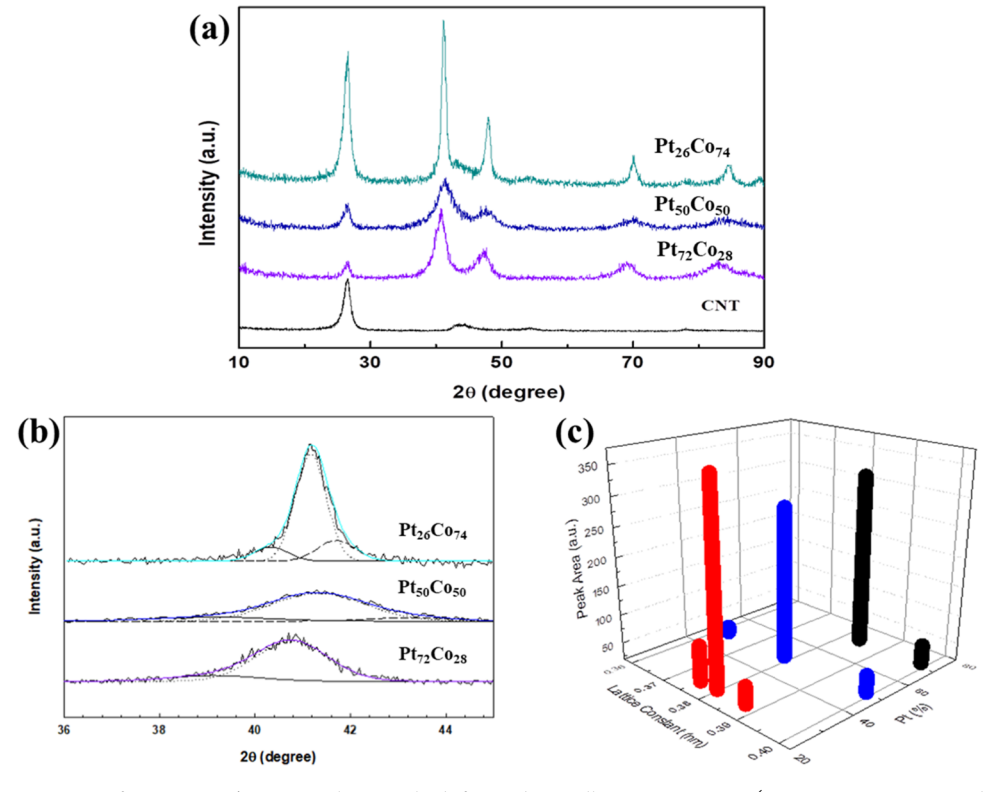


Figure 3. (a) XRD patterns of  $Pt_{100-n}Co_n/CNT$  catalysts with different bimetallic compositions ( $Pt_{26}Co_{74}$ ,  $Pt_{50}Co_{50}$ , and  $Pt_{72}Co_{28}$ ); (b) the deconvolution of the XRD (111) peaks; (c) plot of the deconvoluted peak areas vs the lattice constant corresponding to the peak positions for the catalysts of different bimetallic compositions.

catalyst compositions of the as-obtained  $Pt_nCo_{100-n}/CNT$  were obtained by ICP-OES analysis. For the catalysts synthesized at

 $180\,^{\circ}$ C, the compositions of Co in the catalyst against the feeding ratio are shown in Figure 1a. The linear relationship

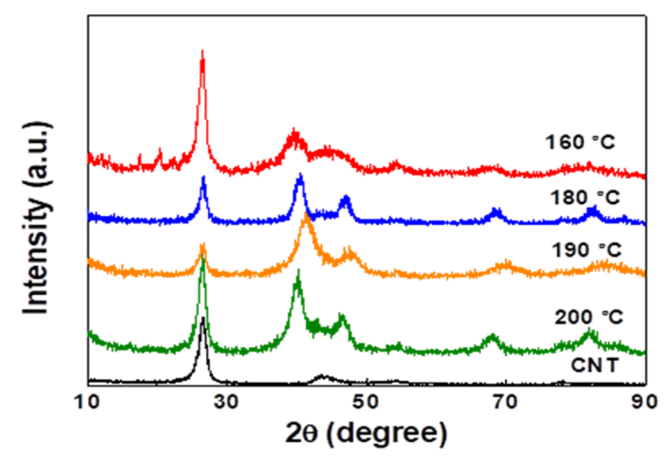
demonstrates that the actual composition of Co in PtCo nanoparticles is highly consistent with the metal precursor feeding composition, indicating that the PtCo nanoalloy composition is controllable at 180 °C. For the catalysts synthesized at different temperatures with the same feeding ratio (50:50), the compositions of Co in the catalyst against the feeding ratio are shown in Figure 1b. In comparison with the 1:1 ratio for the catalyst synthesized at 180 °C, the catalysts synthesized below and above 180 °C showed less Co in the bimetallic nanoalloys.

Figure 2a shows a representative SEM image for  $Pt_{50}Co_{50}/CNT$ . The CNTs feature a porous network of short CNT fibers. Examples of the TEM and HRTEM images are shown in Figure 2b,c. There is a relatively uniform distribution of  $Pt_{50}Co_{50}$  nanoparticles with an average size of  $8.3\pm1.4$  nm on the CNT support. As shown in Figure 1c, both crystalline and amorphous/less-crystalline domains can be clearly identified from the HRTEM (Figure 2c). The lattice fringe of 0.217 nm is characteristic of the (111) plane of the fcc structure. The CNT-supported PtCo NPs feature both amorphous and crystalline morphologies (Figure 2c).

The crystalline structures of the PtCo nanoalloy were further verified by XRD characterization, as shown in Figure 3a. The XRD patterns of PtCo/CNT with a variety of compositions are compared. The peaks at  $\sim$ 27 and  $\sim$ 43° in all of the three samples correspond to the CNT. The diffraction peaks shown at the position of 41, 48, 68, and 81° correspond to the PtCo NPs, which are indexed to (111), (200), and (220) of Pt (PDF No. 04-0802). This result indicates that Pt and Co form a facecentered cubic (fcc) structure. It can also be observed that the position of (111) and (200) peaks shifts to a high angle when the content of Co increases. And the lattice parameters measured from the XRD for Pt<sub>26</sub>Co<sub>74</sub>, Pt<sub>50</sub>Co<sub>50</sub>, and Pt<sub>72</sub>Co<sub>28</sub> are 0.3747, 0.3798, and 0.3882 nm, respectively. All of these are in the range between Pt and Co (Pt 0.3923 nm, Co 0.3545 nm), which indicates that the PtCo nanoalloy is mostly fully alloyed. As the Co atom is smaller than the Pt atom, the Pt crystal cell will shrink when Co is introduced. The deconvolution of the XRD patterns (Figure 3b) indicates that the degree of alloying for Pt<sub>50</sub>Co<sub>50</sub> in terms of the (111) peak position is greater than that for Pt<sub>72</sub>Co<sub>28</sub>, but close to that for Pt<sub>26</sub>Co<sub>74</sub>. This is evidenced by the subtle shift of the dominated peak position, as illustrated in Figure 3c.

The reaction temperature is also shown to affect the phase structure of the nanoalloy. Figure 4 shows a set of XRD patterns for PtCo nanoalloy/CNT catalysts synthesized at different temperatures using the metal precursor ratio of 50:50. These catalysts all show similar main peaks at 41, 48, 68, and 81°, corresponding to the fcc structure. Additional small peaks were observed for the catalyst synthesized at 160 °C, which implies that the PtCo nanoalloy is partially alloyed or has other phases. This is in contrast with the catalysts synthesized at temperatures above 180-190 °C. Except for the Pt<sub>50</sub>Co<sub>50</sub> nanoalloy synthesized at 180 °C, these catalysts exhibited bimetallic compositions with lower Co% (see Figure 1b). For Pt<sub>53</sub>Co<sub>47</sub> and Pt<sub>94</sub>Co<sub>6</sub> which are synthesized under 190 and 200 °C, the (111) peaks are weaker than that of Pt<sub>50</sub>Co<sub>50</sub>, demonstrating that temperatures higher than 200 °C do not favor the alloying of Co with Pt in nanoparticles.

XPS was used to further characterize the chemical state and electronic structure of PtCo nanoalloys. The XPS data analysis and spectral deconvolution were performed using CasaXPS software. Figure 5 shows the representative XPS spectra of



**Figure 4.** XRD patterns of PtCo/CNT catalysts synthesized at different reaction temperatures, which exhibit the bimetallic compositions as shown in Figure 1b.

Pt<sub>50</sub>Co<sub>50</sub>/CNT in the Pt 4f, Co 2p, and O 1s regions. The Pt 4f spectra containing the Pt  $4f_{7/2}$  and Pt  $4f_{5/2}$  states can be deconvoluted into three components. The three pairs of doubles correspond to Pt<sup>0</sup> (71.6 and 74.9 eV, 44.05% peak area), Pt<sup>2+</sup> (72.2 and 75.6 eV, 35.36% peak area), and Pt<sup>4+</sup> (77.5 and 73.5 eV, 20.59% peak area) chemical state, respectively. Similarly, the Co 2p contains three features corresponding to Co<sup>0</sup> (779.4 eV, 55.9% peak area), Co<sup>2+</sup> (782.8 eV, 24.56% peak area), and Co4+ (787.1 eV, 19.45% peak area).25 The majority of the Pt and Co atoms in the PtCo/CNT is characteristic of the zero-valence state. By deconvoluting the O 1s spectrum, the dominant peak is shown at 531.7 eV ((1)), along with a small peak at 534.1 eV ((2))(Figure 5c). The former corresponds to vacancy- or latticetype oxygen species (1), whereas the latter signals the presence of adsorbed OH species (2). The percentages of these two types of oxygen species are 80% (1) and 20% (2), respectively. The changes of the metal oxidation state and relative composition expected for  $Pt_{100-n}Co_n/CNT$  catalysts with other bimetallic compositions were also analyzed. The percentages of zero-valence state Pt and Co are about 70 and 50% or more, respectively, depending on the bimetallic composition (Figure S1). We note that the XPS-determined composition is a relative surface composition since the signal attenuates with the depth. H2-TPR data, as discussed later, provide a good assessment of the oxygen capacity of the

3.2. Assessment of ORR and OER Activities. To gain a general understanding of the electrocatalytic activities of the Pt<sub>100-n</sub>Co<sub>n</sub>/CNT catalysts in the ORR and OER, the catalysts were examined in aqueous electrolytes by standard electrochemical techniques. Rotating disk electrode (RDE) measurements were performed to evaluate the ORR activities of the PtCo catalysts, which were performed in an O2-saturated 0.1 M HClO<sub>4</sub> electrolyte. A presentative set of RDE data for the ORR over PtCo/CNT catalysts of different bimetallic compositions is shown in Figure 6a, along with the mass activity (MA) as a function of composition based on the kinetic currents at 0.900 V (vs RHE) and the mass of Pt in the catalyst (Figure 6a inset). The Pt<sub>50</sub>Co<sub>50</sub>/CNT catalyst shows the highest mass activity (0.61 A mg<sub>Pt</sub><sup>-1</sup>). The overpotential for Pt<sub>50</sub>Co<sub>50</sub>/CNT is similar to that for Pt<sub>26</sub>Co<sub>74</sub>/CNT, but much smaller than Pt<sub>72</sub>Co<sub>28</sub>/CNT. A representative set of

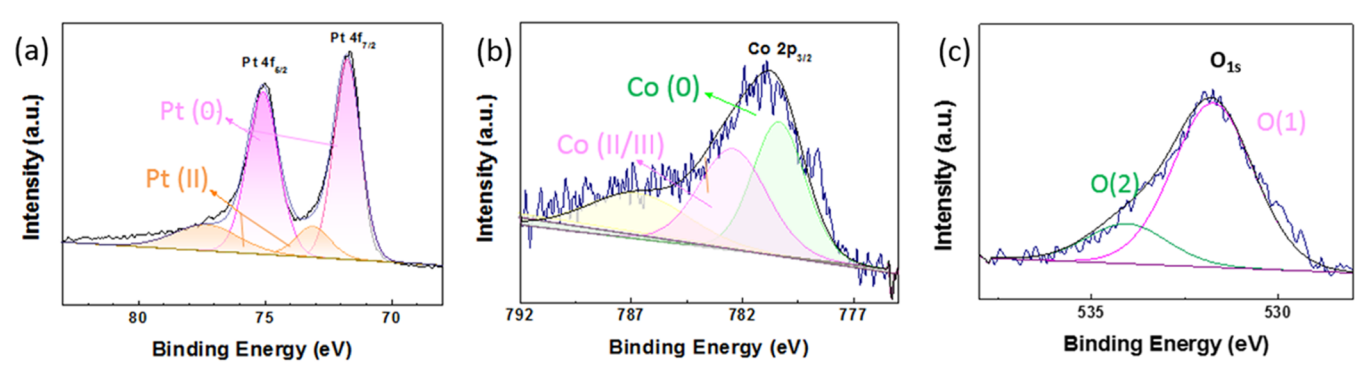


Figure 5. XPS spectra for the  $Pt_{50}Co_{50}/CNT$  catalyst in the regions of (a) Pt 4f, (b) Co 2p, and (c) O 1s. Spectral deconvolutions are shown in the spectra (see Figure S1 for XPS spectra for the catalysts with different compositions).

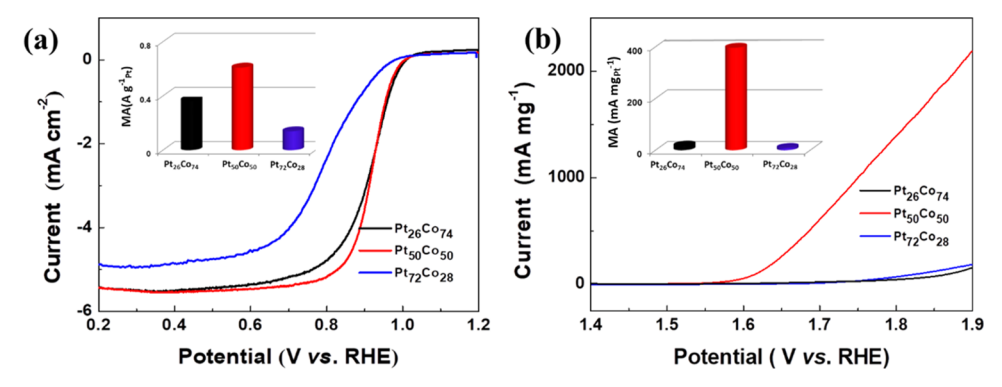


Figure 6. Electrocatalytic characteristics for  $Pt_{100-n}Co_n/CNT$  catalysts of three different compositions: (a) RDE curves for the ORR in  $O_2$ -saturated 0.1 M  $HClO_4$  electrolyte (at a scan rate of 10 mV s<sup>-1</sup> and 1600 rpm). Inset: mass activity (MA) at 0.900 V. (b) Linear voltammetric polarization curves for the OER in 0.1 M  $O_2$ -saturated KOH solution (5 mV s<sup>-1</sup>). Inset: MA at 1.67 V.

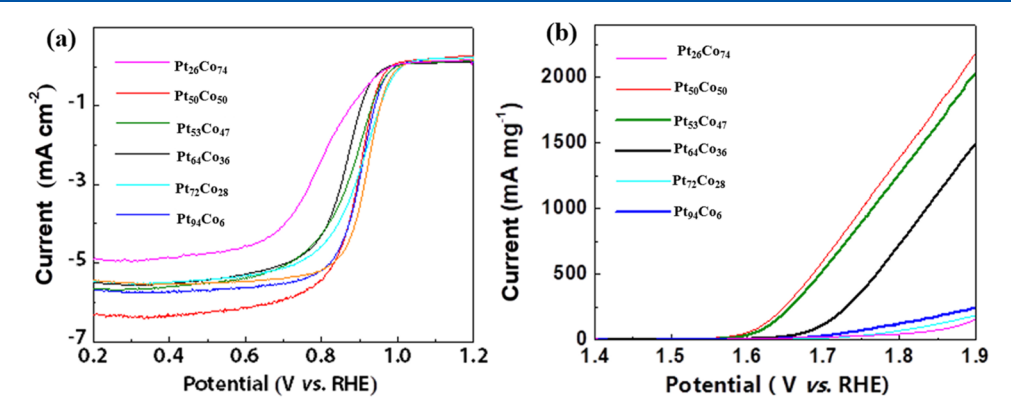


Figure 7. Electrocatalytic characteristics for  $Pt_{100-n}Co_n/CNT$  catalysts of different compositions synthesized at different reaction temperatures which exhibit the different bimetallic compositions as indicated in the plots. (a) RDE curves for the ORR in  $O_2$ -saturated 0.1 M HCl $O_4$  solution (at a scan rate of 10 mV s<sup>-1</sup> and 1600 rpm). (b) Linear voltammetric polarization curves for the OER in 0.1 M  $O_2$  saturated KOH solution (5 mV s<sup>-1</sup>).

voltammetric curves for the OER over the  $Pt_{100-n}Co_n/CNT$  catalysts in 0.1 M  $O_2$  saturated KOH solution is shown in Figure 6b. The electrochemical polarization curves were collected at a scan rate of 5 mV s<sup>-1</sup>. The  $Pt_{50}Co_{50}/CNT$  catalyst shows the highest current density at 1.67 V (396.51 mA mg<sup>-1</sup>). Based on the onset potential of the OER curves, the overpotential for  $Pt_{50}Co_{50}/CNT$  is much smaller than those for  $Pt_{26}Co_{74}/CNT$  and  $Pt_{72}Co_{28}/CNT$ . The ORR and OER activities of the  $Pt_{50}Co_{50}/CNT$  catalyst are indicative of highly active surface active sites due to the synergistic effect of Pt and Co on the surface.

Since the hydrothermal reaction temperature is also an important factor in forming the nanoalloy catalysts during the

hydrothermal process, we also evaluated the ORR and OER activities of the PtCo/CNT catalysts synthesized at different reaction temperatures from 160 to 200 °C (Figure 7a,b). For ORR activity, the Pt<sub>64</sub>Co<sub>36</sub> catalyst synthesized at 160 °C exhibits poor activity. When the temperature reaches 190 °C, even though the composition is similar to that of Pt<sub>50</sub>Co<sub>50</sub>, the activity is less active. Such a difference is indicative of less exposed surface-active sites for Pt<sub>53</sub>Co<sub>47</sub>. For the Pt<sub>96</sub>Co<sub>4</sub> catalyst, the activity is similar to that of the Pt/C catalyst, suggesting the absence of synergistic surface-active sites.

The alloy NPs exhibit electrocatalytic bifunctional activities for charging and discharging (OER/ORR) in a rechargeable  $\text{Li-O}_2$  battery (Figures 6 and 7). The activity is maximized at

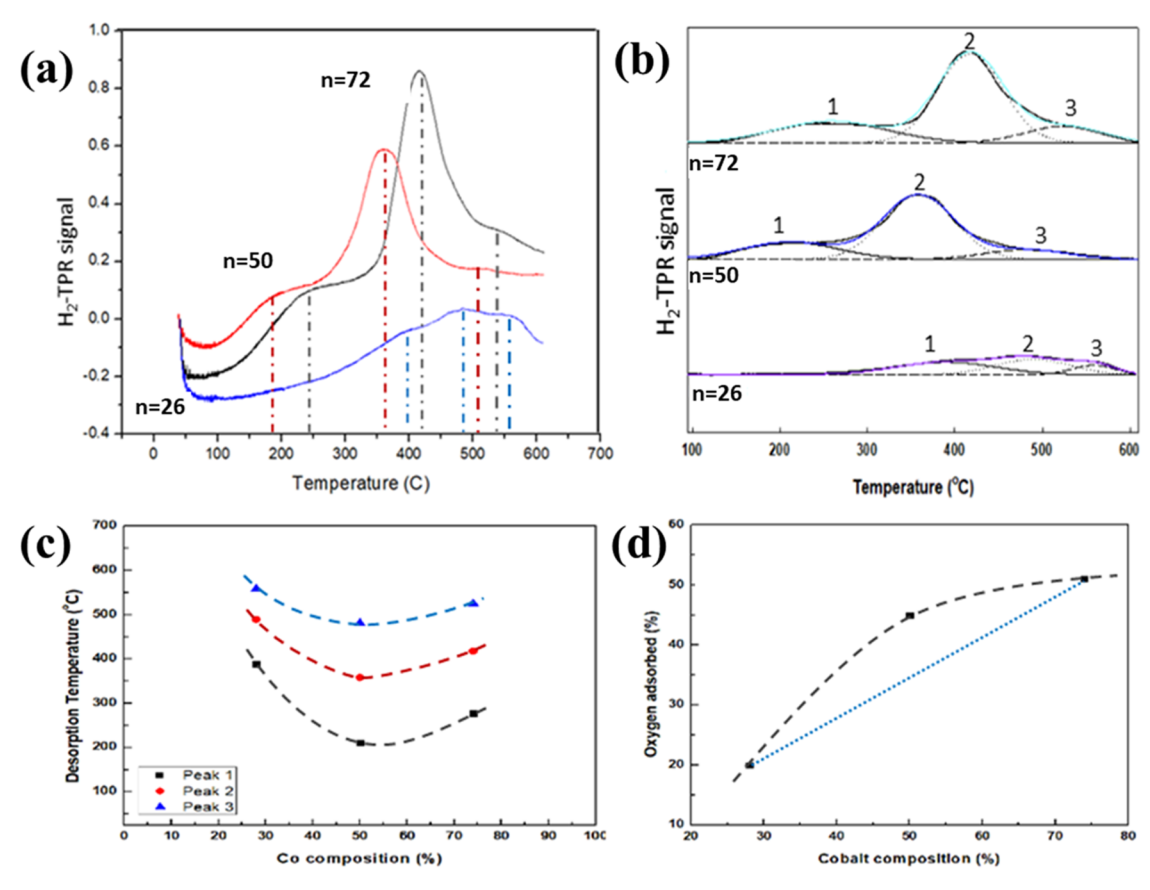


Figure 8. (a)  $H_2$ -TPR curves for the catalysts after oxidation treatment of the  $Pt_{100-n}Co_n/CNT$  (n = 26, 50, and 72) catalysts under  $O_2$  at 260 °C; (b) deconvolution of the TPR curves in panel (a); (c) plots of the deconvoluted peak temperatures vs Co%; and (d) the total oxygen amount in the NPs vs Co%. (The blue dotted line represents a hypothetic linear relationship).

 $Pt_{50}Co_{50}/CNT$ , as evidenced by the reduction of the charging overpotential. Similar bifunctional activities were also observed in previous work for the PdCu/C catalyst in the OER/ORR in a  $Li-O_2$  battery.<sup>17</sup>

3.3. Assessment of Oxygen Adsorption and Release **Capacity.** To further assess the oxygen adsorption and release capacity of the Pt<sub>100-n</sub>Co<sub>n</sub>/CNT catalysts, we performed a H<sub>2</sub>-TPR analysis of the catalysts after oxidation treatment under O<sub>2</sub> at the same temperature (260 °C). Figure 8a shows a representative set of temperature-programmed reduction (TPR) curves, showing reductive desorption peaks at different temperatures. By deconvolution of these curves, each curve reveals three different desorption peaks (Figure 8b). These peak temperatures exhibit a minimum at Pt<sub>50</sub>Co<sub>50</sub> (Figure 8c). By integration of these peaks, the total oxygen amount in the NPs (O%) increases with Co% in PtCo NPs. Rather than a linear relationship, the O% deviates most at Pt<sub>50</sub>Co<sub>50</sub>, showing compositions with  $(Pt_{26}Co_{74})_{1.0}(O)_{0.50}$ ,  $(Pt_{50}Co_{50})_{1.0}(O)_{0.50}$ , and  $(Pt_{72}Co_{28})_{1.0}(O)_{0.50}$ . Clearly, the lowest temperature for the reduction of the metal-oxygen species in Pt<sub>50</sub>Co<sub>50</sub> NPs, which coincides with the maximum amount of oxygen species for Pt<sub>50</sub>Co<sub>50</sub> NPs. This finding may hint at a possible linkage of oxygen adsorption and desorption to the a-/c-phases and the optimal ORR and OER activities for Pt<sub>50</sub>Co<sub>50</sub>/CNT. The oxygen capacity of the catalysts may have played an important role in the catalytic synergy since the activated oxygen species participate in the OER and ORR processes.

To further understand the above results, we performed a density functional theory (DFT) calculation of the adsorption

energy for O and  $O_2$  on the PtCo catalysts of different compositions. Figure 9 shows plots of the adsorption energy vs the composition. The adsorption energies are calculated with O atom and  $O_2$  on  $Pt_xCo_{100-x}$  of different compositions (x = 25, 50, and 75). It is evident that the adsorption energies decrease with Pt%. In comparison with a hypothetic linear

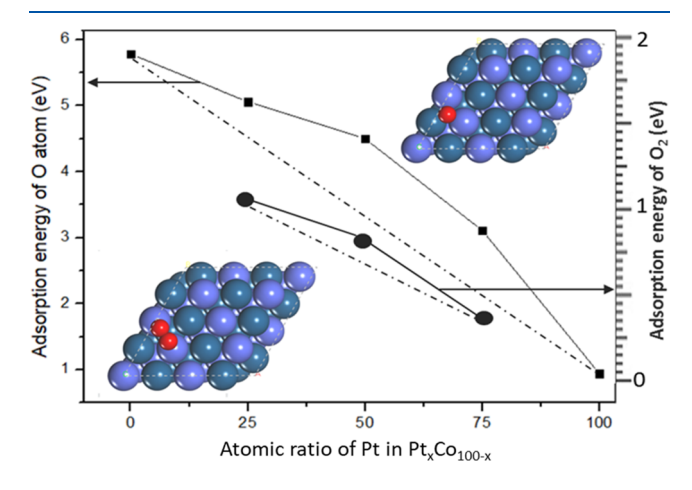


**Figure 9.** Adsorption energies for O atom (filled squares) and  $O_2$  (filled circles) on  $Pt_xCo_{100-x}$  of different compositions (DFT calculation). Inset: O atom (lower left) and  $O_2$  molecule (upper right) adsorptions on a  $Pt_{50}Co_{50}$  alloy model. Dark blue, light blue, and red balls represent Pt, Co, and O atoms, respectively. Dashed lines represent hypothetic linear relationships.

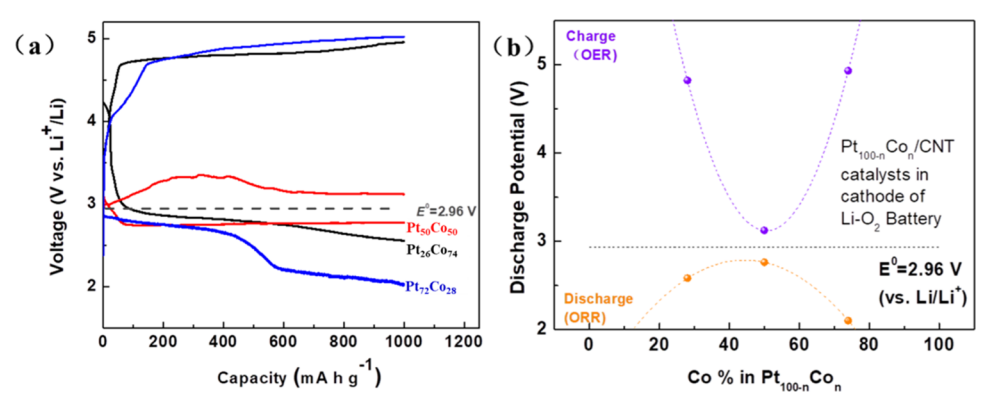


Figure 10. (a) Charge/discharge curves of a Li- $O_2$  battery cell at 100 mA  $g^{-1}$  with  $Pt_{100-n}Co_n/CNT$  catalysts of different compositions synthesized at 180 °C with three different compositions; (b) plots of the charge/discharge potentials as a function of the bimetallic composition for the first cycle. (The horizontal dashed or dotted lines: thermodynamic potential: 2.96 V vs Li<sup>+</sup>/Li for Li<sub>2</sub>O<sub>2</sub> formation).

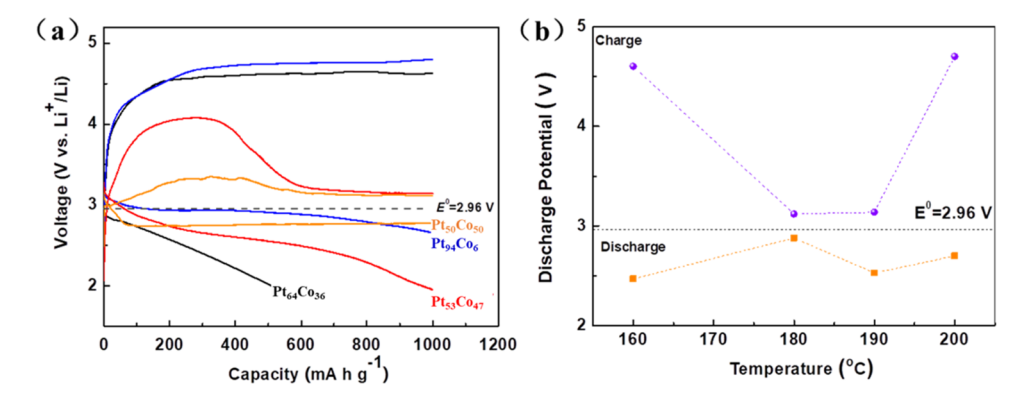


Figure 11. (a) Charge/discharge curves of PtCo/CNT catalysts at 100 mA  $g^{-1}$  synthesized at different temperatures resulting in the different compositions (see Figure 1b). (b) Plots of the charge/discharge potentials as a function of the bimetallic composition for the first cycle. (The horizontal dashed or dotted lines: thermodynamic potential: 2.96 V vs Li<sup>+</sup>/Li for Li<sub>2</sub>O<sub>2</sub> formation).

relationship, the deviations for both O and  $O_2$  occur mostly for  $Pt_{50}Co_{50}$ , which is largely consistent with the  $H_2$ -TPR data (Figure 8c,d). We note that the calculated data are preliminary at this point of time since there are other factors which could affect the catalytic properties, which are part of our ongoing calculation work.

3.4. Li-O<sub>2</sub> Battery Discharging/Charging Character**istics.** The  $Pt_{100-n}Co_n/CNT$  catalysts were examined in a Li-O2 battery cell with LiPF6 in EC/DMC as electrolyte under 100 mA g<sup>-1</sup> and a cutoff capacity of 1000 mA h g<sup>-1</sup>. The discharge-charge curves of a Li-O2 battery strongly depend on the composition of the PtCo/CNT catalysts (Figure 10a). Compared with Pt/C, Pt/CNT, Co/CNT, Pt<sub>26</sub>C<sub>74</sub>/CNT, and Pt<sub>72</sub>Co<sub>28</sub>/CNT catalysts, the Pt<sub>50</sub>Co<sub>50</sub>/CNT catalyst shows the most significant reduction of the overpotentials, as indicated by the observation of 170 mV for ORR overpotential and 160 mV for OER overpotential with respect to the thermodynamic potential. The dependence of the charge/discharge overpotentials on the composition of PtCo/CNT is shown in Figure 10b. It is evident that the charge/discharge overpotential is sensitive to the Co composition and exhibits an apparent minimum in the range of 40-60% Co. There is a synergistic effect of Pt and Co on the ORR/OER performance of the catalysts in the Li-O<sub>2</sub> battery. The fact that the Pt<sub>50</sub>Co<sub>50</sub>/CNT exhibits the lowest charge overpotential suggests the presence of a synergistic pathway for the decomposition and dissolution of the Li<sub>2</sub>O<sub>2</sub> on this bimetallic surface.

The  $Pt_{50}Co_{50}$  catalyst was also tested as a cathode catalyst in the  $Li-O_2$  cell under different charging and discharging current densities. As the current density increases, the overall overpotential of the battery increases due to the polarization effect. However, the high-performance characteristic of the catalyst at high current density remains unchanged.

The catalysts synthesized at different temperatures with the same 50:50 metal feeding ratio, which yield different bimetallic compositions (see Figure 1b), were also examined in the Li–  $O_2$  battery cell (Figure 11). While the ORR overpotentials show insignificant dependence on the synthesis temperature, the OER overpotential strongly depends on the temperature.  $Pt_{53}Co_{47}$  has a composition like  $Pt_{50}Co_{50}$ . They exhibit the comparable charge (OER) overpotential.  $Pt_{64}Co_{36}$  and  $Pt_{53}Co_{47}$  synthesized at temperatures from 160 to 180 °C show much higher OER overpotentials than that for  $Pt_{50}Co_{50}$ . Overall, for the OER, the temperature dependence of the OER overpotential exhibits a minimum near 180 °C, which is similar to the composition dependence of the OER overpotentials shown in Figure 10b.

The above charge/discharge performance test results lead to several important findings. First, there is an extremely low charging overpotential observed for the  $Pt_{50}Co_{50}/CNT$  catalyst on the cathode of the  $Li-O_2$  battery cell, which is 160 mV with respect to the thermodynamic potential. Second, the composition dependence of the activity shows that the  $Pt_{50}Co_{50}/CNT$  catalyst displays optimal performance. Note that these catalysts were not subjected to postsynthesis thermal

treatment. If thermal treatment is applied, the activity showed a noticeable decrease, suggesting the possibility of thermal deactivation of the surface sites, which needs further study to pin down the origin of the deactivation.

### 4. CONCLUSIONS

In conclusion, Pt<sub>100-n</sub>Co<sub>n</sub>/CNT catalysts have been shown to reduce the discharging/charging overpotentials of rechargeable Li-O<sub>2</sub> batteries. The nanoalloys feature both fcc crystalline and less-crystalline/amorphous domains, showing different degrees of oxidation of the Co components in the nanoalloys depending on the bimetallic composition, which is linked to the oxygen capacity of the nanoalloys. The nanoalloy with 50% Co is showing to display an optimal oxygen adsorption and release capacity. By discharging/charging performance testing, the reduction of the overpotentials for the OER and ORR is shown to depend on the bimetallic composition, showing the lowing ORR and OER overpotentials for the Pt<sub>50</sub>Co<sub>50</sub>/CNT catalyst. Most remarkably, the reduction of the overall potential is significant, showing 160 mV higher than the thermodynamic potential, which approaches some of the best catalysts reported in the literature. The linkage of the catalytic synergy to the oxyphilicity of the catalysts is also substantiated by the oxygen adsorption energy. Further refinement of the composition and metal-support interactions is needed, which is part of our ongoing work involving different nanoalloy catalysts and different carbon or other support materials. The rational design and optimization of the morphology, structure, and composition in the nanoalloy catalysts<sup>26</sup> may serve as a new strategy for addressing the confronting passivation and reactivation of the catalyst in the discharging/charging processes.

### ASSOCIATED CONTENT

## Supporting Information

The Supporting Information is available free of charge at https://pubs.acs.org/doi/10.1021/acs.jpcc.3c02890.

Additional XPS data (PDF)

#### AUTHOR INFORMATION

## **Corresponding Author**

Chuan-Jian Zhong — Department of Chemistry, State University of New York at Binghamton, Binghamton, New York 13902, United States; orcid.org/0000-0003-0746-250X; Email: cjzhong@binghamton.edu

#### **Authors**

Ren Na – School of Biological and Environmental Engineering, Tianjin Vocational Institute, Tianjin 300410, China; Department of Chemistry, State University of New York at Binghamton, Binghamton, New York 13902, United States

Merry N. Madiou – Department of Chemistry, State University of New York at Binghamton, Binghamton, New York 13902, United States

**Dominic Caracciolo** – Department of Chemistry, State University of New York at Binghamton, Binghamton, New York 13902, United States

Zhi-Peng Wu — Department of Chemistry, State University of New York at Binghamton, Binghamton, New York 13902, United States Connor Kanyuk — Department of Chemistry, State University of New York at Binghamton, Binghamton, New York 13902, United States

Guojun Shang – Department of Chemistry, State University of New York at Binghamton, Binghamton, New York 13902, United States

Complete contact information is available at: https://pubs.acs.org/10.1021/acs.jpcc.3c02890

#### **Author Contributions**

§Co-first author.

#### Notes

The authors declare no competing financial interest.

### ACKNOWLEDGMENTS

This work was supported by the National Science Foundation (CHE 2102482, and 1566283). The authors thank D. Collins for his assistance in ICP-OES analysis and XRD characterization.

#### REFERENCES

- (1) Kang, J.-H.; Lee, J.; Jung, J.-W.; Park, J.; Jang, T.; Kim, H.-S.; Nam, J.-S.; Lim, H.; Yoon, K. R.; Ryu, W.-H.; et al. Lithium-Air Batteries: Air-Breathing Challenges and Perspective. *ACS Nano* **2020**, *14*, 14549–14578.
- (2) Kwak, W.-J.; Rosy; Sharon, D.; Xia, C.; Kim, H.; Johnson, L. R.; Bruce, P. G.; Nazar, L. F.; Sun, Y.-K.; Frimer, A. A.; et al. Lithium-Oxygen Batteries and Related Systems: Potential, Status, and Future. *Chem. Rev.* **2020**, *120*, *6626*–*6683*.
- (3) Zhang, Q.; Rao, S.; Vummaleti, S. V. C.; Poh, E. T.; Dai, W.; Cui, X.; Wu, J.; Zhang, J.; Chen, W. High-Performance Li-O<sub>2</sub> Batteries Enabled by Dibenzo-24-Crown-8 Aldehyde Derivative as Electrolyte Additives. *Adv. Energy Mater.* **2022**, *12*, No. 2200580.
- (4) Xia, C.; Kwok, C. Y.; Nazar, L. F. A high energy density lithium-oxygen battery based on a reversible four-electron conversion to lithium oxide. *Science* **2018**, *361*, 777–781.
- (5) Zhai, Y.; Yang, W.; Xie, X.; Sun, X.; Wang, J.; Yang, X.; Naik, N.; Kimura, H.; Du, W.; Guo, Z.; et al. Co<sub>3</sub>O<sub>4</sub> nanoparticle-dotted hierarchical-assembled carbon nanosheet framework catalysts with the formation/decomposition mechanisms of Li<sub>2</sub>O<sub>2</sub> for smart lithium—oxygen batteries. *Inorg. Chem. Front.* **2022**, *9*, 1115–1124.
- (6) Wang, K.-X.; Zhu, Q.-C.; Chen, J.-S. Strategies toward High-Performance Cathode Materials for Lithium—Oxygen Batteries. *Small* **2018**, *14*, No. 1800078.
- (7) Dang, C.; Mu, Q.; Xie, X.; Sun, X.; Yang, X.; Zhang, Y.; Maganti, S.; Huang, M.; Jiang, Q.; Seok, I.; et al. Recent progress in cathode catalyst for nonaqueous lithium oxygen batteries: a review. *Adv. Compos. Hybrid Mater.* **2022**, *5*, 606–626.
- (8) Liu, J.; Zhang, T.; Waterhouse, G. I. N. Complex alloy nanostructures as advanced catalysts for oxygen electrocatalysis: from materials design to applications. *J. Mater. Chem. A* **2020**, *8*, 23142–23161
- (9) Huang, J.; Jin, Z.; Xu, Z.-L.; Qin, L.; Huang, H.; Sadighi, Z.; Yao, S.; Cui, J.; Huang, B.; Kim, J.-K. Porous RuO2 nanosheet/CNT electrodes for DMSO-based Li-O<sub>2</sub> and Li ion O<sub>2</sub> batteries. *Energy Storage Mater.* **2017**, *8*, 110–118.
- (10) Zheng, M.; Jiang, J.; Lin, Z.; He, P.; Shi, Y.; Zhou, H. Stable Voltage Cutoff Cycle Cathode with Tunable and Ordered Porous Structure for Li-O<sub>2</sub> Batteries. *Small* **2018**, *14*, No. e1803607.
- (11) Lai, W. H.; Zhang, B. W.; Hu, Z.; Qu, X. M.; Jiang, Y. X.; Wang, Y. X.; Wang, J. Z.; Liu, H. K.; Chou, S. The Quasi-Pt-Allotrope Catalyst: Hollow PtCo@single-Atom Pt<sub>1</sub> on Nitrogen-Doped Carbon toward Superior Oxygen Reduction. *Adv. Funct. Mater.* **2019**, 29, No. 1807340.
- (12) Luo, W.-B.; Gao, X.-W.; Chou, S.-L.; Wang, J.-Z.; Liu, H.-K. Porous AgPd-Pd Composite Nanotubes as Highly Efficient Electro-

- catalysts for Lithium-Oxygen Batteries. Adv. Mater. 2015, 27, 6862-6869.
- (13) Su, D.; Kim, H.-S.; Kim, W.-S.; Wang, G. A study of  $Pt_xCo_y$  alloy nanoparticles as cathode catalysts for lithium-air batteries with improved catalytic activity. *J. Power Sources* **2013**, 244, 488–493.
- (14) Lu, Y.-C.; Xu, Z.; Gasteiger, H. A.; Chen, S.; Hamad-Schifferli, K.; Shao-Horn, Y. Platinum-Gold Nanoparticles: A Highly Active Bifunctional Electrocatalyst for Rechargeable Lithium-Air Batteries. *J. Am. Chem. Soc.* **2010**, *132*, 12170–12171.
- (15) Yin, J.; Fang, B.; Luo, J.; Wanjala, B.; Mott, D.; Loukrakpam, R.; Ng, M. S.; Li, Z.; Hong, J.; Whittingham, M. S.; et al. Nanoscale alloying effect of gold—platinum nanoparticles as cathode catalysts on the performance of a rechargeable lithium-oxygen battery. *Nanotechnology* **2012**, *23*, No. 305404.
- (16) Yin, J.; Fang, B.; Luo, J.; Wanjala, B.; Mott, D.; Loukrakpam, R.; Ng, M. S.; Li, Z.; Hong, J.; Whittingham, M S.; Zhong, C.-J. Nanoscale Alloying Effect of Gold-Platinum Nanoparticles as Cathode Catalysts on the Performance of a Rechargeable Lithium-Oxygen Battery. *Nanotechnology* **2012**, *23*, 305404.
- (17) Kang, N.; Ng, M. S.; Shan, S.; Wu, J.; Zhao, W.; Yin, J.; Fang, W.; Luo, J.; Petkov, V.; Zhong, C.-J. Synergistic catalytic properties of bifunctional nanoalloy catalysts in rechargeable lithium-oxygen battery. *J. Power Sources* **2016**, *326*, 60–69.
- (18) Ding, S.; Yu, X.; Ma, Z.-F.; Yuan, X. A review of rechargeable aprotic lithium-oxygen batteries based on theoretical and computational investigations. *J. Mater. Chem. A* **2021**, *9*, 8160–8194.
- (19) Tang, W.; Teng, K.; Guo, W.; Gu, F.; Li, B.; Qi, R.; Liu, R.; Lin, Y.; Wu, M.; Chen, Y. Defect-Engineered Co<sub>3</sub>O<sub>4</sub>@Nitrogen-Deficient Graphitic Carbon Nitride as an Efficient Bifunctional Electrocatalyst for High-Performance Metal-Air Batteries. *Small* **2022**, *18*, No. 2202194.
- (20) Liang, H.; Jia, L.; Chen, F.; Jing, S.; Tsiakaras, P. A novel efficient electrocatalyst for oxygen reduction and oxygen evolution reaction in Li-O<sub>2</sub> batteries: Co/CoSe embedded N, Se co-doped carbon. *Appl. Catal., B* **2022**, *317*, No. 121698.
- (21) Wang, P.; Ren, Y.; Wang, R.; Zhang, P.; Ding, M.; Li, C.; Zhao, D.; Qian, Z.; Zhang, Z.; Zhang, L.; Yin, L. Atomically dispersed cobalt catalyst anchored on nitrogen-doped carbon nanosheets for lithium-oxygen batteries. *Nat. Commun.* **2020**, *11*, No. 1576.
- (22) Wang, W.; Cai, J.; Wan, H.; Cai, W.; Zhu, Z.; Wang, C.; Zhou, T.; Hou, Z.; Zhu, Y.; Qian, Y. Electron-redistributed Ni-Co oxide nanoarrays as an ORR/OER bifunctional catalyst for low overpotential and long lifespan Li-O<sub>2</sub> batteries. *J. Mater. Chem. A* **2022**, *10*, 14613–14621.
- (23) Hou, C.; Han, J.; Liu, P.; Yang, C.; Huang, G.; Fujita, T.; Hirata, A.; Chen, M. Operando observations of  $RuO_2$  catalyzed  $Li_2O_2$  formation and decomposition in a Li- $O_2$  micro-battery. *Nano Energy* **2018**, 47, 427–433.
- (24) Luo, W. B.; Pham, T. V.; Guo, H. P.; Liu, H. K.; Dou, S. X. Three-Dimensional Array of TiN@Pt<sub>3</sub>Cu Nanowires as an Efficient Porous Electrode for the Lithium-Oxygen Battery. *ACS Nano* **2017**, *11*, 1747–1754.
- (25) Xing, Y.; Chen, N.; Luo, M.; Sun, Y.; Yang, Y.; Qian, J.; Li, L.; Guo, S.; Chen, R.; Wu, F. Long-life lithium-O<sub>2</sub> battery achieved by integrating quasi-solid electrolyte and highly active Pt<sub>3</sub>Co nanowires catalyst. *Energy Storage Mater.* **2020**, *24*, 707–713.
- (26) Wu, Z.-P.; Shan, S.; Zang, S.-Q.; Zhong, C.-J. Dynamic Core—Shell and Alloy Structures of Multimetallic Nanomaterials and Their Catalytic Synergies. *Acc. Chem. Res* **2020**, *53*, 2913–2924.